



CdS/CdSe co-sensitized brookite H:TiO₂ nanostructures: Charge carrier dynamics and photoelectrochemical hydrogen generation



Yung-Shan Chang^a, Mingi Choi^b, Minki Baek^b, Ping-Yen Hsieh^a, Kijung Yong^{b,*}, Yung-Jung Hsu^{a,*}

^a Department of Materials Science and Engineering, National Chiao Tung University, Hsinchu 30010, Taiwan

^b Surface Chemistry Laboratory of Electronic Materials, Department of Chemical Engineering, Pohang University of Science and Technology (POSTECH), Pohang 790-784, Korea

ARTICLE INFO

Keywords:
Brookite TiO₂
Hydrogen doping
Sensitization
Interfacial charge dynamics
PEC hydrogen production

ABSTRACT

In this study, we have synthesized CdS/CdSe co-sensitized brookite TiO₂ nanostructures with hydrogen doping (H:TiO₂/CdS/CdSe) in a facile solution reaction and studied their PEC performances. Compared to undoped brookite TiO₂, the H:TiO₂/CdS/CdSe composites exhibit much enhanced photocurrent generation, which originates from the improved charge transfer kinetics endowed by hydrogen doping and sensitization. Time-resolved photoluminescence (PL) and electrochemical impedance spectroscopy (EIS) are employed to explore the charge transfer dynamics between sensitizers and TiO₂ and charge carrier kinetics at the semiconductor/electrolyte interface. According to the analytical results, sensitizations of TiO₂ are found to enhance the charge separation efficiency. Besides, the hydrogen doping into TiO₂ generates oxygen vacancy states, providing additional charge transfer pathway and prohibiting charge recombination, beneficial for enhancing the PEC performances as well. Based on the charge dynamics data, we further develop charge transfer models for TiO₂/CdS/CdSe and H:TiO₂/CdS/CdSe. The findings from this work can help understanding the charge transfer dynamics in brookite TiO₂-based composite systems as well as designing versatile photoelectrodes for solar energy conversion.

1. Introduction

Since Fujishima and Honda have discovered the photoactivity of TiO₂ [1], TiO₂ has been intensively investigated as a photocatalyst for photolysis and a photoelectrode for solar energy conversion. TiO₂ is known to have three main polymorphs: anatase, rutile, and brookite. Among these crystal phases, brookite is the least explored in both fundamental and application studies. In our previous work [2], we successfully synthesized brookite TiO₂ nanobullet arrays with a facile solution reaction method. The synthesized brookite TiO₂ outperforms anatase and rutile TiO₂ in photoelectrochemical (PEC) activity. However, the reason for such enhanced PEC performances is still not clear. Although the electron lifetime of brookite TiO₂ is found to be longer than anatase and rutile TiO₂, the charge transfer dynamics are still not fully understood yet. Since charge transfer dynamics play a key role in determining the performance of semiconductors in photoconversion processes [3–12], it is necessary to explore charge transfer dynamics in such a kind of newly developed photoelectrodes.

Doping of TiO₂ with hydrogen [13–15] has attracted much attention because the hydrogen doping introduces extra states in TiO₂, which significantly changes the band structure and enables TiO₂ to absorb

sunlight in the visible region. In addition, it increases the density of oxygen vacancies, increasing the electrical conductivity to facilitate charge transportation. Inspired by this necessity, we have synthesized the hydrogen-doped brookite TiO₂ for application in PEC water splitting [16]. Due to the increased conductivity and narrowed bandgap, hydrogen-doped TiO₂ showed enhanced photocurrent generation compared to the undoped TiO₂.

In this work, we have co-sensitized hydrogen-doped brookite TiO₂ with CdS and CdSe in order to improve the visible light absorption and enhance PEC performances. CdS and CdSe are two promising materials that have been extensively used as sensitizers for metal oxide photoanodes [17–20]. Because they have relatively small band gaps and well-aligned band structures with metal oxides, the resultant nanocomposites have demonstrated significantly enhanced PEC efficiency. Several studies have reported the combination of TiO₂ and CdS/CdSe [21,22], but these works are all related to rutile or anatase TiO₂. The sensitization of brookite TiO₂ is scarcely studied, not even to mention about the hydrogen-doped ones. In the present study, we have systematically investigated the PEC performances and charge transfer dynamics for the hydrogen-doped, sensitized brookite TiO₂. Time-resolved photoluminescence (PL) and electrochemical impedance spectroscopy (EIS)

* Corresponding authors.

E-mail addresses: kyong@postech.ac.kr (K. Yong), yhsu@cc.nctu.edu.tw, yhsu@mail.nctu.edu.tw (Y.-J. Hsu).

are employed to explore the charge transfer dynamics at the heterojunction and semiconductor/electrolyte interface [23–26]. From the time-resolved PL and EIS results, we have constructed a scheme of charge carrier transfer for the sensitized brookite TiO_2 and also evaluated the charge dynamics parameters such as carrier lifetime and charge transfer rate constant.

2. Experimental section

2.1. Chemicals

All the chemicals were analytical grade and used without further purification. Special care should be taken when dealing with the hazardous Cd source.

2.2. Synthesis of brookite TiO_2 nanobullet arrays

The brookite TiO_2 nanobullet arrays were synthesized by following the method reported in our previous work [2]. First, the titanium foil was sequentially cleaned in acetone, ethanol and deionized water under ultrasonication for 10 min. The cleaned titanium foil was dried in the air and then put into the autoclave filled with 0.1 M sodium hydroxide solution (70 mL). The autoclave was heated in an oven at 220 °C for 24 h. The as-obtained sample was immersed in the 1 M hydrochloric acid (100 mL) for 10 min and then rinsed with deionized water and ethanol. Finally, the sample was annealed in a muffle furnace at 500 °C for 4 h at a ramping rate of 2 °C min⁻¹, producing brookite TiO_2 nanobullet arrays.

2.3. Synthesis of hydrogen-doped brookite TiO_2 nanobullet arrays

The synthesis of hydrogen-doped brookite TiO_2 nanobullet arrays also follows the method reported in our previous work [16]. For hydrogen doping, the TiO_2 nanobullet arrays were annealed in a tubular furnace for 2 h at 700 °C at a ramping rate of 5 °C min⁻¹ in a 4% H₂/96% N₂ mixed gas flow. When the apparent color of the samples turns white, the hydrogen doping is finished. In the following paragraph, the hydrogen-doped brookite TiO_2 was denoted as H:TiO₂.

2.4. Deposition of CdS on brookite TiO_2 and H:TiO₂

To deposit CdS quantum dots on the surface of TiO_2 , successive ionic layer adsorption and reaction (SILAR) method was used [27]. First, 4.59 g of cadmium sulfate and 5.28 g of sodium sulfide as a precursor of Cd²⁺ and S²⁻ were respectively dissolved in 110 mL of deionized water. Afterwards, TiO_2 and H:TiO₂ samples were immersed in the cadmium sulfate solution (0.2 M) for 30 s. The samples were then rinsed with deionized water and immersed into sodium sulfide solution (0.2 M) for another 30 s. A 30-s immersion in cadmium sulfate followed by a 30-s immersion in sodium sulfide makes one cycle of SILAR. Samples of 20-cycle deposition and 30-cycle deposition were prepared and denoted as TiO₂/CdS_20C and TiO₂/CdS_30C, respectively in the latter paragraph.

2.5. Deposition of CdSe on TiO_2/CdS and H:TiO₂/CdS

Chemical bath deposition (CBD) method was used for the deposition of CdSe [28]. A 0.5 mM of sodium selenosulphate was used as a precursor of Se²⁻, while a 4.7 mM cadmium acetate dihydrate was used as a precursor of Cd²⁺. To deposit CdSe on the surface of TiO_2/CdS and H:TiO₂/CdS, the TiO₂/CdS and H:TiO₂/CdS samples were put into the solution composed of 10 mL of Cd²⁺ precursor, 150 μL of ammonia hydroxide (99%) and 10 mL of Se²⁻ precursor. The mixed solution was put into an oven at 95 °C for 3 h. The whole procedure was repeated for three times. Herein, four CdSe-deposited samples were prepared, which are denoted as TiO₂/CdS/CdSe_20C, TiO₂/CdS/CdSe_30C, H:TiO₂/CdS/CdSe_20C, and H:TiO₂/CdS/CdSe_30C.

2.6. Characterizations

The morphology of the prepared samples was observed by the field-emission scanning electron microscope (FE-SEM, Philips, XL30S) operated at 5.0 kV and high-resolution scanning transmission electron microscope (Cs-corrected HR-STEM, JEOL JEM-2200FS). The crystallographic structure was studied with X-ray diffraction (XRD, Rigaku, D/MAX-2500). The elemental analysis was conducted using the energy dispersive X-ray spectrometry (EDS), the accessory of HR-STEM. The elemental depth profiles were collected with the secondary ion mass spectrometry (SIMS, Cameca, IMS 6f). A Cs⁺ primary ion beam with impact energy of 5 keV and a beam current of 50 nA were applied to analyze the samples. The chemical states were recorded by X-ray photoelectron spectroscopy (XPS, VG Scientific, ESCA LAB 250). A monochromatic Al K α radiation was used as the excitation source. The binding energies of the recorded spectra were calibrated by C 1s peak at 284.4 eV. The UV-vis absorption spectroscopy data were collected by a spectrometer (Shimadzu, UV2501PC) attached with an ISR-2200 integrating sphere. Time-resolved PL data were collected by an inverted-type scanning confocal microscope (Picoquant, MicroTime-200) with a 20X objective. For time-resolved PL measurement, the excitation source was a 375 nm single-mode pulsed diode laser which delivered ~100 ps pulse width at a 5–20 MHz repetition rate. The time-correlated single-photon counting (TCSPC) technique was used to obtain the PL decay kinetics as a function of time. Exponential fitting for the obtained PL decay profiles was performed by Symphotime software (version 5.3). The PEC measurements were conducted in a typical three-electrode potentiostat system (EG&G Princeton Applied Research, model 263A,) under one-sun irradiation (AM 1.5G, 100 mW/cm²). Ag/AgCl was used as a reference electrode and a platinum mesh was used as counter electrode. 0.25 M Na₂S/0.35 M Na₂SO₃ was used as electrolyte. The data of EIS were collected under open-circuit potential, with the frequency range from 1 MHz to 100 mHz and the 10 mV of AC signal. The incident photon-to-current efficiency (IPCE) data were collected at 0 V vs Ag/AgCl. The hydrogen evolution test was conducted at 1.23 V vs RHE in 0.5 M Na₂SO₃. The other experimental conditions for EIS, IPCE and hydrogen evolution tests were identical to those for PEC measurements. The dye adsorption experiments were performed by immersing the electrodes in the rhodamine B solution (RhB, 5.0 mL, 0.025 mM) under darkness condition. At a given time interval, the electrodes were taken out and the RhB solution was analyzed with UV-vis absorption spectroscopy to record the concentration variation of RhB.

3. Results and discussion

Fig. 1(a)–(d) shows the morphology of four different samples, which are pristine brookite TiO_2 , H:TiO₂, H:TiO₂/CdS, and H:TiO₂/CdS/CdSe, respectively. The SEM image in **Fig. 1(a)** shows that brookite TiO_2 has a bullet-shape structure with a length of 700–1000 nm and width 150–250 nm. By comparing **Fig. 1(a)** and (b), we find that there is no obvious difference between pristine TiO_2 and H:TiO₂ in morphology, showing that the shape of TiO_2 does not change after hydrogen doping. The deposition of CdS on the H:TiO₂ nanobullet arrays is confirmed in **Fig. 1(c)**, showing a rough surface with small nanoparticles loaded. CdS quantum dots are directly deposited on the surface of H:TiO₂ through SILAR method. The sizes of CdS quantum dots are around 5–10 nm. Subsequently, CdSe quantum dots are directly grown on H:TiO₂/CdS through CBD and the resultant morphology is shown in **Fig. 1(d)**. The sizes of CdSe quantum dots are about 10–20 nm. Further crystallographic structures are studied by XRD in **Fig. 1(e)**. Because all the samples are grown on the titanium foil, the peaks from titanium are also found as marked with yellow circles, which correspond to (100), (002) and (101) planes (JCPDS #44-1294). The diffraction peaks of brookite TiO_2 are all in good agreement with standard pattern (JCPDS #76-1934). One thing worthy of note is that there is no noticeable change in

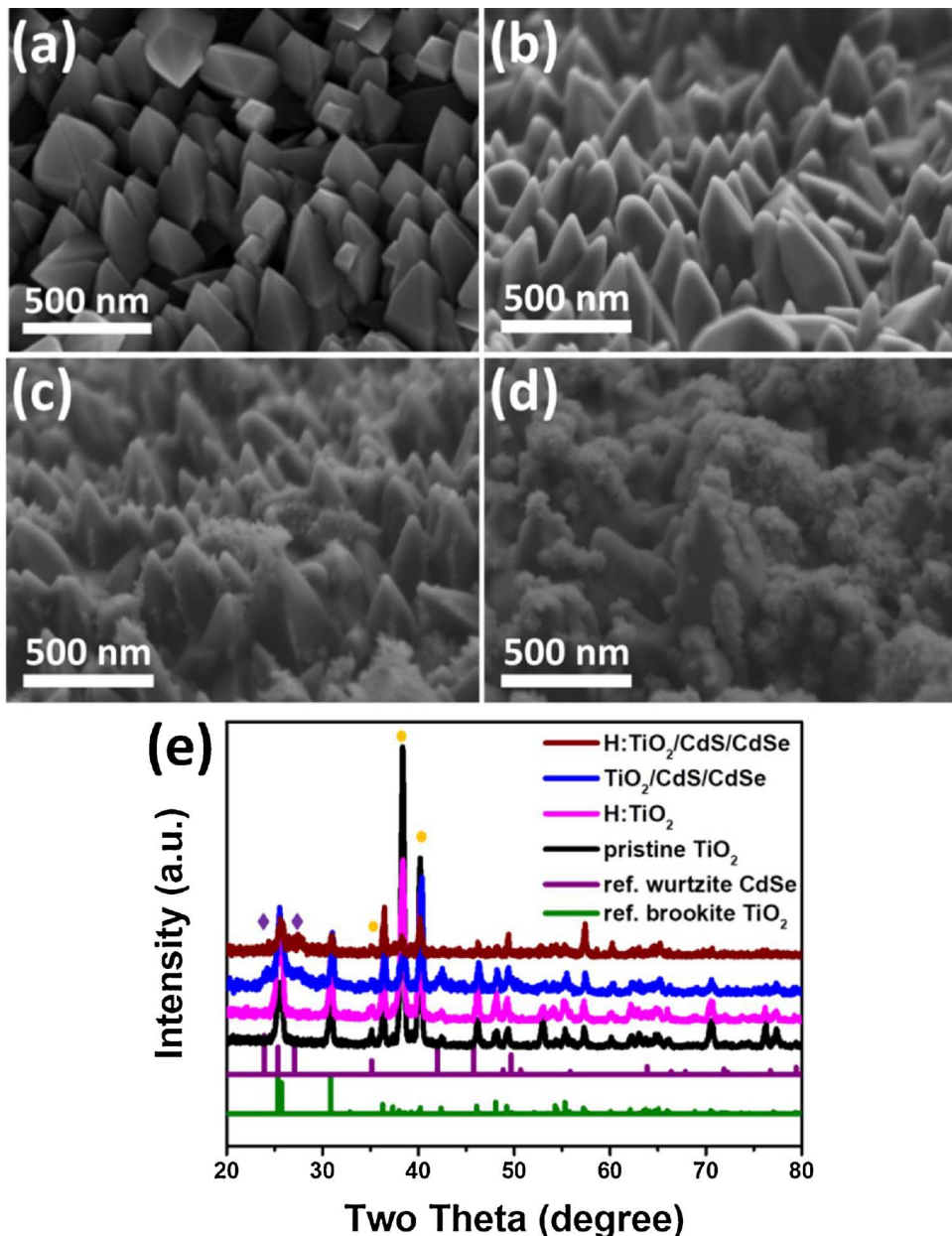


Fig. 1. Tilted-angle SEM images of (a) pristine TiO₂, (b) H:TiO₂ (c) H:TiO₂/CdS, and (d) H:TiO₂/CdSe. (e) shows the corresponding XRD patterns. Yellow circles and purple diamonds indicate diffraction peaks from titanium foil and CdSe, respectively. (For interpretation of the references to colour in this figure legend, the reader is referred to the web version of this article.)

XRD pattern between pristine TiO₂ and H:TiO₂, indicating that the doping of hydrogen does not influence the lattice structure of TiO₂. The peaks at $2\theta = 23.9^\circ$ and 27.1° , which are marked with purple diamonds, could be attributed to the diffraction plane of (100) and (101) of CdSe, respectively (JCPDS #08-0459). However, because CdSe quantum dots are quite small in size and thus the signals are very weak with a broad feature. On the other hand, it is hard to observe the XRD signals of Cds since Cds quantum dots are mostly covered by CdSe.

Detailed lattice fringe observation and EDS analysis were obtained by HR-STEM. Fig. 2(a) shows the lattice fringe of H:TiO₂/CdS/CdSe, which is the magnification of the place marked by black square in Fig. 2(b) of TEM image. The lattice spacing of brookite TiO₂ is 0.22 nm, which could be assigned to the plane (202). The lattice spacing of CdS is 0.25 nm, which is assigned to the plane (102). As for CdSe, the lattice spacing assigned to plane (100) is 0.37 nm. Fig. 2(b) is the TEM image with lower magnification and its EDS spectra. From the elemental mapping of EDS, elements of TiO₂ are well confirmed. One interesting finding is that the areal distributions of S and Se are quite similar, which provides a strong proof that CdSe quantum dots

are mostly deposited on the top of CdS, which can act as nucleation sites for CdSe.

The chemical states and hydrogen dopant content of H:TiO₂ were studied with SIMS and XPS. Fig. 3(a) and (b) compare the SIMS depth profiles for pristine TiO₂ and H:TiO₂. The hydrogen traces observed for pristine TiO₂ originate from the hydrochloric acid treatment during the preparation process. In comparison with pristine TiO₂, H:TiO₂ displays a more significant increase in hydrogen content inside the structure, reflecting the successful hydrogen doping for H:TiO₂. Fig. 3(c) and (d) further show the Ti 2p and O 1s XPS spectra for the two samples. The nearly identical Ti 2p spectra for pristine TiO₂ and H:TiO₂ suggest that hydrogen ions are incorporated at the interstitial sites of TiO₂ [16]. The O 1s spectra further reveal the higher peak intensity of O–H component for H:TiO₂ as a result of hydrogen doping. Comparing the peak area of O–H component between H:TiO₂ and pristine TiO₂ gives a nominal hydrogen dopant content of around 2.2 at% for H:TiO₂.

The optical properties of H:TiO₂ and the sensitized samples were investigated by UV-vis absorption spectroscopy. Compared to undoped brookite TiO₂ showing an absorption below 380 nm (inset in Fig. 4(a))

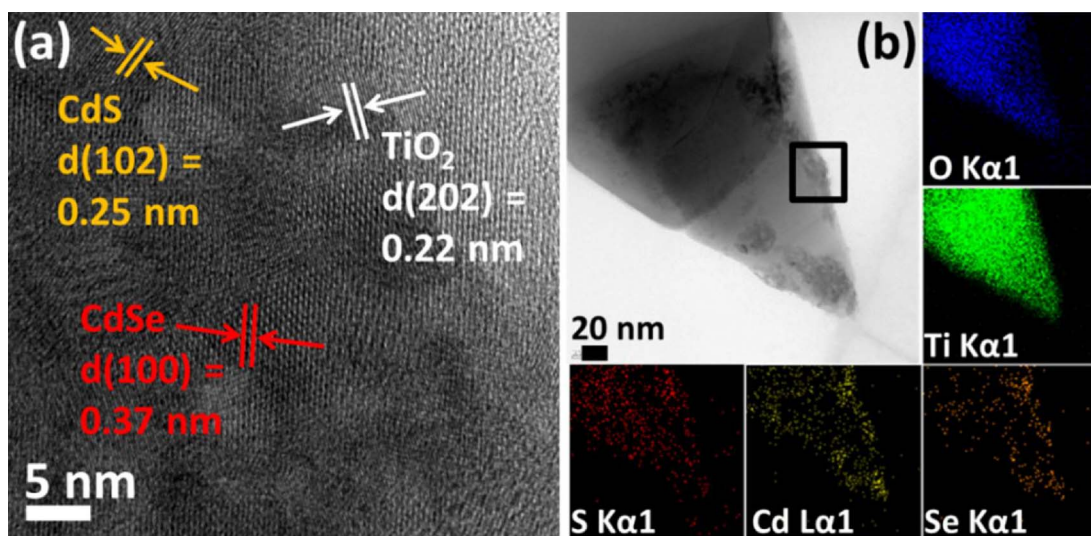


Fig. 2. (a) HRTEM image of H:TiO₂/CdS/CdSe. (b) TEM image and elemental mapping from EDS of H:TiO₂/CdS/CdSe.

[2,16], the H:TiO₂ exhibits a slight red shift of absorption edge toward 400 nm. This shift could be attributed to the extra state introduced by the hydrogen doping. With the deposition of CdS, both TiO₂/CdS and H:TiO₂/CdS show extended light absorption to around 550 nm, which is due to the low bandgap of CdS ($E_g = 2.25$ eV). The subsequent growth of CdSe on TiO₂/CdS further extend the light absorption edge to 650 nm caused by lower bandgap of CdSe ($E_g = 1.90$ eV). The optical bandgaps were determined from Tauc plot, which is provided in Fig. 4(b). This extended light absorption of co-sensitized TiO₂ is one of the main reasons that lead to the enhancement of the PEC performances.

The PEC performances of the prepared samples were studied by acquiring linear-sweep voltammetry curves. The measurements were conducted from –1.2 to 0.5 V vs Ag/AgCl under one-sun illumination. Fig. 5(a) shows that with the deposition of CdS quantum dots on TiO₂, the photocurrent is slightly enhanced. The increased SILAR cycle number of CdS from 20 to 30 further increases the photocurrent. The

TiO₂/CdS_30C generates a photocurrent of around 0.2 mA/cm² at 0 V vs Ag/AgCl, which is about two times higher than the photocurrent of TiO₂/CdS_20C. This is due to higher loading of CdS on TiO₂ [29]. As a result, all the samples used in the latter measurement were deposited with 30 cycles of SILAR growth for CdS. A more drastic extent of photocurrent increase was observed when CdSe was deposited on TiO₂/CdS. This phenomenon could be attributed to an extensive light absorption and enhanced charge separation, which will be later confirmed by time-resolved PL and EIS data. As seen in Fig. 5(a), the photocurrent of TiO₂/CdS/CdSe_30C reaches 1.7 mA/cm², which is about 10 times higher than TiO₂/CdS and also around 1.7 times higher than TiO₂/CdS/CdSe_20C.

The effects of hydrogen doping on PEC performance were also studied and the results are presented in Fig. 5(b) as a comparison with undoped ones. The H:TiO₂ nanostructure and its sensitized composites all show the enhanced PEC performances than the undoped counterparts. The photocurrent of H:TiO₂/CdS/CdSe increases up to 2.8 mA/

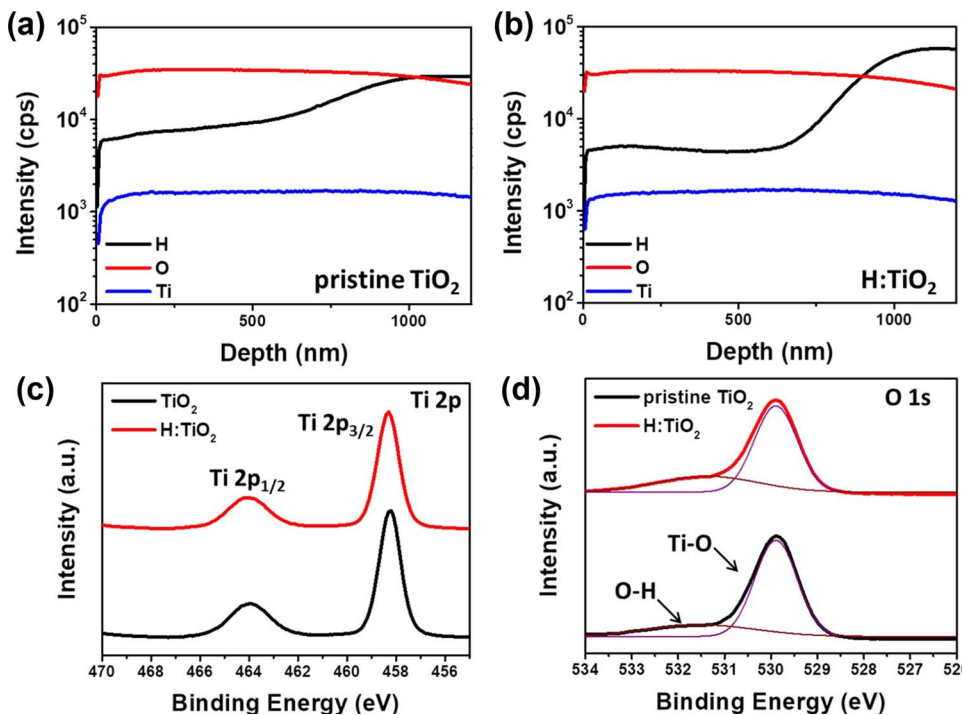


Fig. 3. SIMS depth profiles recorded on (a) pristine TiO₂ and (b) H:TiO₂. (c) and (d) show the corresponding Ti 2p and O 1s XPS spectra, respectively.

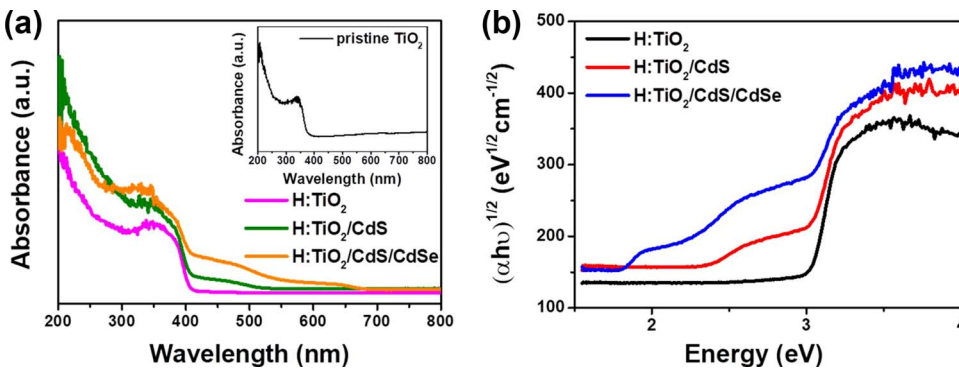


Fig. 4. (a) UV-vis absorption spectra of H:TiO₂, H:TiO₂/CdS, and H:TiO₂/CdS/CdSe. Inset is the absorption spectrum of pristine TiO₂. (b) Corresponding Tauc plots for determination of bandgap.

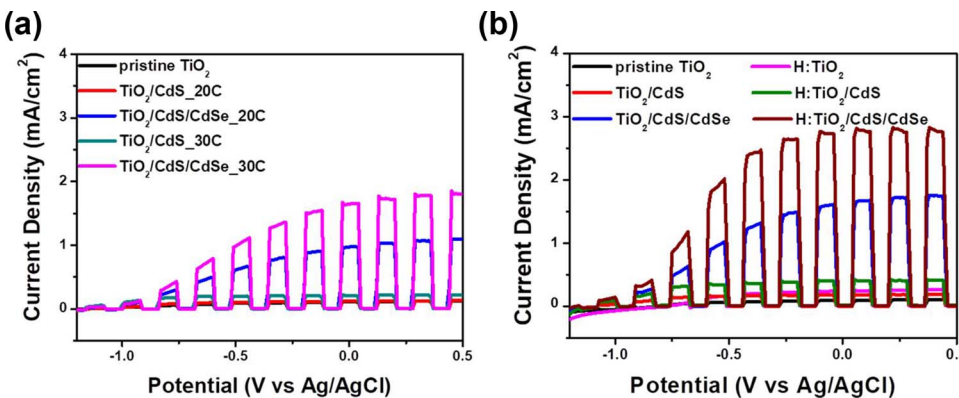


Fig. 5. (a) Linear-sweep voltammetry curves of pristine TiO₂ and those sensitized with CdS and CdS/CdSe with different SILAR cycles. (b) Linear-sweep voltammetry of pristine TiO₂, TiO₂/CdS, TiO₂/CdS/CdSe, H:TiO₂, H:TiO₂/CdS, and H:TiO₂/CdS/CdSe.

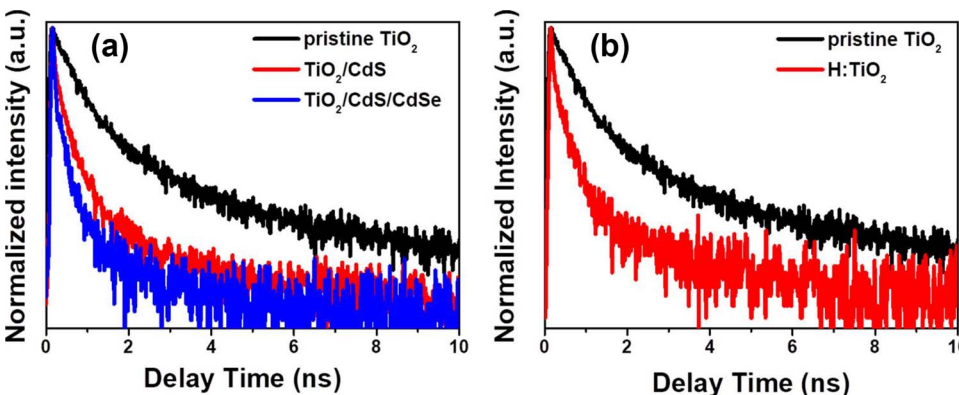


Fig. 6. (a) Time-resolved PL spectra of pristine TiO₂, TiO₂/CdS, TiO₂/CdS/CdSe collected at 500 nm. (b) Time-resolved PL spectra of pristine TiO₂ and H:TiO₂ collected at 500 nm.

cm^2 , which is much improved compared to TiO₂/CdS/CdSe. These results could be attributed to the extensive light absorption and increased conductivity induced by hydrogen doping. In addition, improved charge separation also contributes to these results, which will be further discussed in the time-resolved PL measurement. On the other hand, the CdS/CdSe co-sensitized samples surpass the single-sensitized ones (Fig. S1) in photocurrent generation, illustrating the beneficial, synergistic feature of CdS/CdSe co-sensitizing for enhancing the PEC performance of pristine TiO₂ and H:TiO₂.

Time-resolved PL is one of the powerful techniques to study the charge transfer dynamics. In this study, charge transfer kinetics of the sensitized brookite TiO₂ were studied by time-resolved PL. The charge transfer rate constant at the heterojunction interface can be determined through the formula [30–33]:

$$k_{\text{ct}} = 1 / \langle \tau_2 \rangle - 1 / \langle \tau_1 \rangle$$

where k_{ct} is the rate constant of charge transfer between the sensitizer and the TiO₂, while $\langle \tau_1 \rangle$ and $\langle \tau_2 \rangle$ are the carrier lifetime of

pristine TiO₂ and sensitized TiO₂, respectively. By using the formula above, the k_{ct} of TiO₂/CdS and TiO₂/CdS/CdSe in Fig. 6(a) are calculated to be $2.06 \times 10^9 \text{ s}^{-1}$ and $4.67 \times 10^9 \text{ s}^{-1}$, respectively. These quantified results provide strong evidence that a deposition of CdSe helps charge transfer in TiO₂ nanocomposites. The time-resolved PL comparison of TiO₂ and H:TiO₂ was also performed and the results are shown in Fig. 6(b). Fig. 6(b) collects the emission from 500 nm, which is contributed by TiO₂. Due to the extra states introduced by hydrogen doping, many excited electrons are trapped in the introduced states and thus reduce the recombination of electron-hole pairs. As a result, a faster decay of PL was observed. These charge dynamics results well match with the results of PEC that a greater amount of charge carriers are separated at the interface for H:TiO₂ composites than for TiO₂ composites. Detailed fitting results are provided in the supporting information (Table S1).

EIS is another powerful method to study the charge transfer dynamics, especially at the interface between semiconductor and electrolyte. The semicircles in Fig. 7 represent the resistances at the

interface between photoanode and electrolyte. The equivalent circuit used for fitting is shown in the inset. In this circuit, R_s stands for series resistance in the circuit, R_{ct} and C_{ct} represent the charge transfer resistance and capacitance between the photoanode and redox couple. Fig. 7(a) shows that pristine TiO_2 has the largest semicircle, whose resistance of charge transfer (R_{ct}) is fitted as 182,000 Ω , which is rather high. With the deposition of CdS and CdSe, the radius of semicircle is decreased, having R_{ct} values of 31,746 Ω and 15,243 Ω , respectively. This is due to enhanced charge separation and therefore reduced charge transfer resistance. Similar results are also found for H: TiO_2 samples, as shown in Fig. 7(b). The radius of semicircle is decreased when the CdS and CdSe are sequentially deposited on the surface of H: TiO_2 to accelerate charge transfer. The corresponding values of charge transfer resistance are provided in supporting information (Table S2). One thing worthy of note is that the H: TiO_2 nanocomposites all have smaller resistances compared to the undoped counterparts. Since the charge separation efficiency between CdS and CdSe does not depend on doping of TiO_2 , these differences originate from the introduction of extra states in the band gap of H: TiO_2 , which enable extra excitons to accumulate at the interface at photoanode and electrolyte. The more excitons generated in H: TiO_2 than in TiO_2 was confirmed by the Mott-Schottky analysis in our previous work [16]. In addition to interfacial charge dynamics, the influence of surface area on the PEC performance also needs to be considered. Because the samples prepared in this work are directly grown on the supporting substrate, it is impractical to measure the surface area with the typical N_2 adsorption-desorption technique which is specifically designed for powder specimens. To estimate the effective surface area, here we performed the dye adsorption experiments by immersing the electrodes in the rhodamine B (RhB) solution and probing the amount of RhB adsorbed. Higher RhB adsorption amount signifies larger effective surface area for the electrodes. As Fig. S2 and Table S3 summarize, the amount of RhB adsorbed is comparable for the relevant samples. For example, after immersed in the dark for 12 h, 1.60 and 1.56 pmol of RhB is adsorbed by $\text{TiO}_2/\text{CdS}/\text{CdSe}$ and H: $\text{TiO}_2/\text{CdS}/\text{CdSe}$, respectively, suggesting that the effective surface

areas of the two samples are commensurate. Although the estimation of surface area from dye adsorption data may not be accurate, the results provide a tentative index to evaluate the value of effective surface area for the samples [34,35]. The demonstration from the RhB adsorption experiments suggests that the observed photoactivity enhancement for H: $\text{TiO}_2/\text{CdS}/\text{CdSe}$ is not related to the structural factors regarding surface area, but stems from the improved interfacial charge transfer as a result of hydrogen doping.

To further understand the dependence of PEC performances on illumination wavelength, we conducted IPCE measurements. As can be seen in Fig. 8(a), the pristine TiO_2 shows photoactivity at wavelength below 380 nm. With the deposition of CdS and CdSe, the photoactivity is red-shifted to a longer wavelength, which well matches the outcomes shown in UV-vis absorption measurement. Compared to the undoped TiO_2 , the H: TiO_2 and its sensitized composites all show enhanced conversion efficiencies, which could be attributed to the improved charge transfer kinetics endowed by hydrogen doping and sensitization, confirmed by time-resolved PL and EIS results. The practical hydrogen evolution was also estimated by conducting PEC water splitting at 1.23 V vs RHE. Fig. 8(b) compares the theoretical H_2 gas evolution rates calculated from photocurrents and the measured H_2 evolution amount for H: TiO_2 and H: $\text{TiO}_2/\text{CdS}/\text{CdSe}$. Both samples show good match in theoretical and measured hydrogen production rates, while H: $\text{TiO}_2/\text{CdS}/\text{CdSe}$ sample shows higher H_2 evolution rate as expected from PEC results. The Faradic efficiency (η) can be evaluated from the following equation [36],

$$\eta = \frac{\text{volume of gas (experimental)}}{\text{volume of gas (theoretical)}} = \frac{\text{volume of gas (experimental)}}{\frac{R \times T \times I \times t}{p \times z \times F}}$$

where R , T , I , t , p , z , F correspond to ideal gas constant, temperature of gas, photocurrent, time, pressure, number of electrons for releasing one molecule of gas (2 for hydrogen gas) and the Faraday constant, respectively. The calculated results are shown in supporting information (Table S4). The obtained η values are all higher than 90%, indicating that hydrogen gas is generated in a very efficient way.

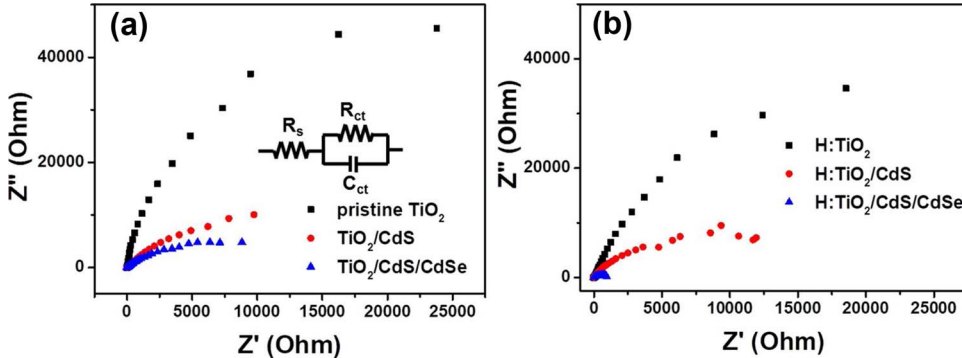


Fig. 7. (a) EIS data of pristine TiO_2 , TiO_2/CdS , and $\text{TiO}_2/\text{CdS}/\text{CdSe}$. Inset is the fitted equivalent circuit. (b) EIS data of H: TiO_2 , H: TiO_2/CdS , and H: $\text{TiO}_2/\text{CdS}/\text{CdSe}$.

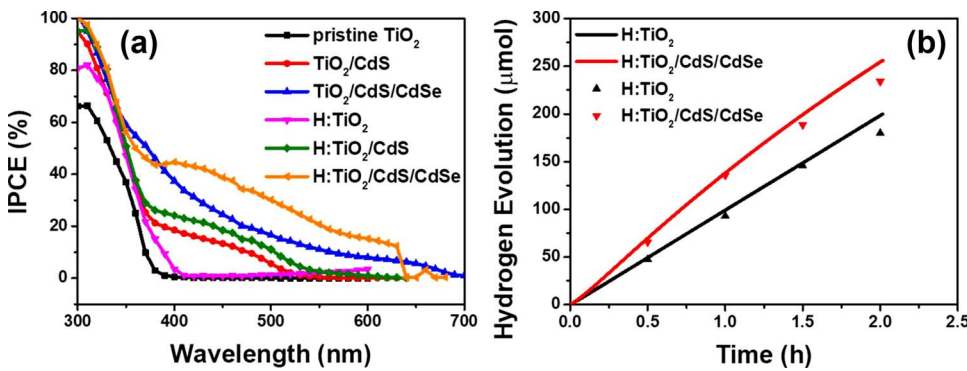


Fig. 8. (a) IPCE spectra of pristine TiO_2 , TiO_2/CdS , $\text{TiO}_2/\text{CdS}/\text{CdSe}$, H: TiO_2 , H: TiO_2/CdS and H: $\text{TiO}_2/\text{CdS}/\text{CdSe}$. (b) Hydrogen evolution tests on H: TiO_2 and H: $\text{TiO}_2/\text{CdS}/\text{CdSe}$. The solid curves represent the theoretical values of hydrogen amount produced.

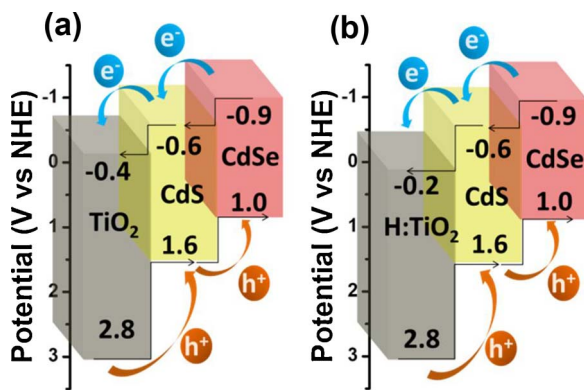


Fig. 9. Proposed charge transfer mechanism for TiO₂/CdS/CdSe and H:TiO₂/CdS/CdSe.

Based on time-resolved PL and EIS results, we propose charge transfer mechanisms for TiO₂/CdS/CdSe and H:TiO₂/CdS/CdSe. As shown in Fig. 9, when the CdS and CdSe quantum dots are deposited on the surface of TiO₂, electrons will transfer from CdSe through CdS to TiO₂ in a stepwise type-II band alignment configuration [37,38]. Then the electrons will relax to fluorescent trap state and recombine with holes at valence state. On the other hand, holes will transfer in the opposite direction from TiO₂ through CdS to CdSe. As for the hydrogen doped TiO₂, according to our previous work [16], the doping of hydrogen atoms into TiO₂ introduces extra states, which can reduce the bandgap of TiO₂ and thus extend the light absorption range. In addition, the introduction of extra states also helps in promoting charge separation, which was the main reason that H:TiO₂-based composites always have better performance than the undoped TiO₂ counterparts.

4. Conclusion

Among the three main polymorphs of TiO₂, brookite TiO₂ is rarely studied. Especially, the sensitization of H:TiO₂ has never been reported yet. In the present study, we have prepared brookite TiO₂ and hydrogen-doped brookite TiO₂ nanobullet arrays co-sensitized with CdS and CdSe quantum dots, and evaluated their PEC hydrogen generation performances. Due to efficient charge transfer/separation by ideally aligned band structure, H:TiO₂/CdS/CdSe produces a photocurrent as high as 2.8 mA/cm², which is much higher than the undoped counterparts. The results of time-resolved PL and EIS analyses suggest that sensitization and hydrogen doping improves charge transfer and charge separation, accountable for the much enhanced PEC performance of H:TiO₂/CdS/CdSe. Hydrogen evolution tests further illustrate the promising potentials of H:TiO₂/CdS/CdSe for practical solar water splitting.

Acknowledgements

This work was financially supported by the Ministry of Science and Technology of Taiwan (MOST 104-2923-E-009-005-MY2 and 105-2119-M-009-003) and the National Research Foundation of Korea

(NRF-2015K2A1B8047058, NRF-2016R1A4A1010735, NRF-2016R1A2B2011416).

Appendix A. Supplementary data

Supplementary data associated with this article can be found, in the online version, at <https://doi.org/10.1016/j.apcatb.2017.11.063>.

References

- [1] A. Fujishima, K. Honda, Nature 238 (1972) 37–38.
- [2] M. Choi, K. Yong, Nanoscale 6 (2014) 13900–13909.
- [3] T.-T. Yang, W.-T. Chen, Y.-J. Hsu, K.-H. Wei, T.-Y. Lin, T.-W. Lin, J. Phys. Chem. C 114 (2010) 11414–11420.
- [4] Y.-F. Lin, Y.-J. Hsu, Appl. Catal. B 130–131 (2013) 93–98.
- [5] W.-H. Lin, T.-F.M. Chang, Y.-H. Lu, T. Sato, M. Sone, K.-H. Wei, Y.-J. Hsu, J. Phys. Chem. C 117 (2013) 25596–25603.
- [6] Y.-H. Lu, W.-H. Lin, C.-Y. Yang, Y.-H. Chiu, Y.-C. Pu, M.-H. Lee, Y.-C. Tseng, Y.-J. Hsu, Nanoscale 6 (2014) 8796–8803.
- [7] Y.-C. Chen, K.-I. Katsumata, Y.-H. Chiu, K. Okada, N. Matsushita, Y.-J. Hsu, Appl. Catal. A 490 (2015) 1–9.
- [8] Y.-C. Pu, W.-H. Lin, Y.-J. Hsu, Appl. Catal. B 163 (2015) 343–351.
- [9] Y.-C. Chen, T.-C. Liu, Y.-J. Hsu, ACS Appl. Mater. Interfaces 7 (2015) 1616–1623.
- [10] J.-M. Li, H.-Y. Cheng, Y.-H. Chiu, Y.-J. Hsu, Nanoscale 8 (2016) 15720–15729.
- [11] W.-H. Lin, Y.-H. Chiu, P.-W. Shao, Y.-J. Hsu, ACS Appl. Mater. Interfaces 8 (2016) 32754–32763.
- [12] Y.-C. Pu, H.-Y. Chou, W.-S. Kuo, K.-H. Wei, Y.-J. Hsu, Appl. Catal. B 204 (2017) 21–32.
- [13] G. Wang, H. Wang, Y. Ling, Y. Tang, X. Yang, R.C. Fitzmorris, C. Wang, J.Z. Zhang, Y. Li, Nano Lett. 11 (2011) 3026–3033.
- [14] M.C. Wu, C.H. Chen, W.K. Huang, K.C. Hsiao, T.H. Lin, S.H. Chan, P.Y. Wu, C.F. Lu, Y.H. Chang, T.F. Lin, K.H. Hsu, J.F. Hsu, K.M. Lee, J.J. Shyue, K. Kordás, W.F. Su, Sci. Rep. 7 (2017) 40896–40907.
- [15] G.D. Bromiley, A.A. Shiryaev, Phys. Chem. Miner. 33 (2006) 426–434.
- [16] M. Choi, J.H. Lee, Y.J. Jang, D. Kim, J.S. Lee, H.M. Jang, K. Yong, Sci. Rep. 6 (2016) 36099–36110.
- [17] H.B. Yang, J. Miao, S.-F. Hung, F. Huo, H.M. Chen, B. Liu, ACS Nano 8 (2014) 10403–10413.
- [18] J. Hensel, G. Wang, Y. Li, J.Z. Zhang, Nano Lett. 10 (2010) 478–483.
- [19] G. Wang, X. Yang, F. Qian, J.Z. Zhang, Y. Li, Nano Lett. 10 (2010) 1088–1092.
- [20] H. Kim, M. Seol, J. Lee, K. Yong, J. Phys. Chem. C 115 (2011) 25429–25436.
- [21] G. Zhu, L. Pan, T. Xu, Z. Sun, ACS Appl. Mater. Interfaces 3 (2011) 3146–3151.
- [22] S.A. Pawara, D.S. Patilb, H.R. Junga, J.Y. Parka, S.S. Malic, C.K. Hongc, J.C. Shinc, P.S. Patild, J.H. Kim, Electrochim. Acta 203 (2016) 74–83.
- [23] J.S. Yang, P.W. Liao, J.J. Wu, ACS Appl. Mater. Interfaces 5 (2013) 7425–7431.
- [24] L. Wang, G. Tian, Y. Chen, Y. Xiao, H. Fu, Nanoscale 8 (2016) 9366–9375.
- [25] C.J. Chen, P.T. Chen, M. Basu, K.C. Yang, Y.R. Lu, C.L. Dong, C.G. Ma, C.C. Shen, S.F. Hu, R.S. Liu, J. Mater. Chem. A 3 (2015) 23466–23476.
- [26] J. Zhang, Q. Zhang, L. Wang, X. Li, W. Huang, Sci. Rep. 6 (2016) 27241–27250.
- [27] W. Kim, M. Baek, K. Yong, Sens. Actuators B Chem. 223 (2016) 599–605.
- [28] Z. Zhang, M. Choi, M. Baek, K. Yong, Adv. Mater. Interfaces 3 (2016) 1500737–1500746.
- [29] J. Luo, L. Ma, T. He, C.F. Ng, S. Wang, H. Sun, H. Fan, J. Phys. Chem. C 116 (2012) 11956–11963.
- [30] Y.-C. Chen, Y.-C. Pu, Y.-J. Hsu, J. Phys. Chem. C 116 (2012) 2967–2975.
- [31] M.-Y. Chen, Y.-J. Hsu, Nanoscale 5 (2013) 363–368.
- [32] K.-A. Tsai, Y.-J. Hsu, Appl. Catal. B 164 (2015) 271–278.
- [33] Y.-H. Chiu, Y.-J. Hsu, Nano Energy 31 (2017) 286–295.
- [34] C.H. Giles, A.J. Groszek, Proc. Soc. Anal. Chem. 6 (1969) 83–85.
- [35] D.L. Postai, C.A. Demarchi, F. Zanatta, D.C.C. Melo, C.A. Rodrigues, Alexandria Eng. J. 55 (2016) 1713–1723.
- [36] D.A. Wheeler, Y. Ling, R.J. Dillon, R.C. Fitzmorris, C.G. Dudzik, L. Zavodivker, T. Rajh, N.M. Dimitrijevic, G. Millhauser, C. Bardeen, Y. Li, J.Z. Zhang, J. Phys. Chem. C 117 (2013) 26821–26830.
- [37] T.H. Thanh, D.H. Thanh, V.Q. Lam, Adv. Optoelectron. 2014 (2014) 397681.
- [38] J. Yan, Q. Ye, F. Zhou, RSC Adv. 2 (2012) 3978–3985.